nature physics

ARTICLES

https://doi.org/10.1038/s41567-020-01104-z

Check for updates

A charge-density-wave topological semimetal

Wujun Shi[1,2,10], Benjamin J. Wieder[3,10], Holger L. Meyerheim[4,10], Yan Sun[1], Yang Zhang[1,5], Yiwei Li[6], Lei Shen[7], Yanpeng Qi[2], Lexian Yang[7], Jagannath Jena[4], Peter Werner[4], Klaus Koepernik[5], Stuart Parkin[4], Yulin Chen[2,6,7], Claudia Felser[1], B. Andrei Bernevig[3]✉ and Zhijun Wang[8,9]✉

Topological physics and strong electron–electron correlations in quantum materials are typically studied independently. However, there have been rapid recent developments in quantum materials in which topological phase transitions emerge when the single-particle band structure is modified by strong interactions. Here we demonstrate that the room-temperature phase of $(TaSe_4)_2I$ is a Weyl semimetal with 24 pairs of Weyl nodes. Owing to its quasi-one-dimensional structure, $(TaSe_4)_2I$ also hosts an established charge-density wave instability just below room temperature. We show that the charge-density wave in $(TaSe_4)_2I$ couples the bulk Weyl points and opens a bandgap. The correlation-driven topological phase transition in $(TaSe_4)_2I$ provides a route towards observing condensed-matter realizations of axion electrodynamics in the gapped regime, topological chiral response effects in the semimetallic phase, and represents an avenue for exploring the interplay of correlations and topology in a solid-state material.

Conventional solid-state Weyl semimetals[1–12] are three-dimensional (3D) materials whose bulk Fermi pockets derive from linearly dispersing, point-like nodal degeneracies. Unlike in other solid-state semimetals with lower dimensionality or higher symmetry[13–16], the Fermi pockets of 3D Weyl semimetals carry integer-valued topological (chiral) charges, reflecting that the nodal points are sources and sinks of Berry curvature[1]. Because the low-energy spectra of the nodal points in Weyl semimetals resemble the Weyl equation in high-energy physics, the nodal points have become known as condensed-matter Weyl points (WPs)[1–12].

In Weyl semimetals, the surface projections of WPs of opposite chirality are connected by topological surface Fermi arcs[1]. These surface Fermi arcs have emerged as the primary experimental means of confirming the presence of bulk WPs, and their signatures have been observed in angle-resolved photoemission spectroscopy (ARPES) experiments[2–10,17–21] and scanning tunnelling microscopy probes of quasiparticle interference[22,23]. Researchers have also proposed bulk probes of chiral topology in Weyl semimetals, including the intrinsic spin Hall effect[24], the anomalous Hall effect[25,26] and the quantized circular photogalvanic effect[27].

Most interestingly, although the above response effects can be understood from the perspective of single-particle physics, researchers have also proposed more exotic response effects in Weyl semimetals with significant electron–electron interactions. For example, in several theoretical proposals[28–30], attractive electron–electron interactions have been shown to drive a Weyl semimetal into a topological superconductor. Even in the absence of superconductivity, interactions can still drive a Weyl semimetal into a (generically incommensurate) charge-density wave (CDW) phase in which the CDW wavevectors 'nest' bulk WPs. If the nested WPs carry the same chiral charges, the CDW may access a gapless topological phase with monopole harmonic order[31], and if the nested WPs carry opposite chiral charges, the CDW may access a gapped phase in which dynamical CDW angle defects bind chiral modes as a result of effective axion electrodynamics[32,33]. Although there has been substantial recent interest in measuring unconventional superconductivity and axionic response effects, the relative dearth of candidate Weyl semimetals with interacting instabilities has hindered the confirmation of these theoretical proposals.

In this Article, we make a link between non-interacting and correlated Weyl semimetals by employing first-principles calculations and experimental probes to demonstrate that quasi-1D $(TaSe_4)_2I$ crystals[34] are in fact Weyl semimetals whose WPs become coupled and gapped by the onset of a CDW. Although the high-temperature phase of $(TaSe_4)_2I$ has previously been highlighted for exhibiting linear crossings near the Fermi energy (E_F)[35,36] and Kramers–Weyl fermions far below E_F (ref. [37]), our work shows that $(TaSe_4)_2I$ hosts topological chiral fermions at E_F, and reports a link between the bulk WPs and the CDW wavevectors. Furthermore, because $(TaSe_4)_2I$ crystallizes in chiral space group (SG) 97 ($I422$), it hosts WPs with opposite chiral charges at different energies[27,37,38] and therefore provides a promising platform for the observation of bulk probes of topological chirality[27]. In $(TaSe_4)_2I$, we find that all of the Fermi pockets originate from Bloch states that lie within a small energy range of the nodes of 48 WPs, which we designate as the Fermi-surface WPs (FSWPs). The 48 FSWPs specifically lie within 15 meV of E_F: 16 $C=+1$ FSWPs lie ~9 meV below E_F, and the remaining 32 lie above. The net +16 chiral charge of the WPs below E_F is the largest value thus far predicted in a real material.

Previous experiments have shown that $(TaSe_4)_2I$ transitions into an incommensurate, gapped CDW phase when cooled just below room temperature[39–41]. Using first-principles calculations, we compute the high-density electronic susceptibility and FSWP nesting vectors (Supplementary Sections A and G, respectively). We then performed

[1]Max Planck Institute for Chemical Physics of Solids, Dresden, Germany. [2]School of Physical Science and Technology, ShanghaiTech University, Shanghai, China. [3]Department of Physics, Princeton University, Princeton, NJ, USA. [4]Max Planck Institute of Microstructure Physics, Halle (Saale), Germany. [5]Leibniz Institute for Solid State and Materials Research, Dresden, Germany. [6]Department of Physics, University of Oxford, Oxford, UK. [7]State Key Laboratory of Low Dimensional Quantum Physics, Department of Physics and Collaborative Innovation Center of Quantum Matter, Tsinghua University, Beijing, China. [8]Beijing National Laboratory for Condensed Matter Physics, and Institute of Physics, Chinese Academy of Sciences, Beijing, China. [9]University of Chinese Academy of Sciences, Beijing, China. [10]These authors contributed equally: Wujun Shi, Benjamin J. Wieder, Holger L. Meyerheim. ✉e-mail: bernevig@princeton.edu; wzj@iphy.ac.cn

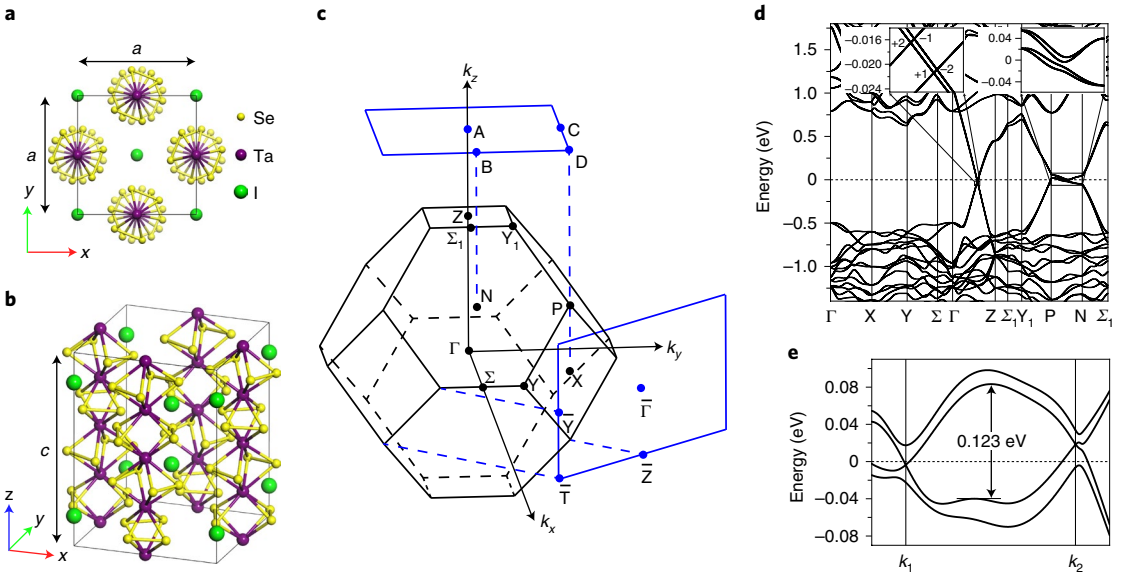

Fig. 1 | Crystal structure, 3D bulk and 2D surface Brillouin zones and electronic structure of $(TaSe_4)_2I$. a,**b**, The crystal structure is shown from both top (001) (**a**) and tilted side (**b**) perspectives, where, throughout this work, surface terminations are labelled using the conventional-cell lattice vectors (a, a, c). Because $(TaSe_4)_2I$ crystallizes in the body-centred tetragonal space group 97 ($I422$)[34], its primitive cell contains half as many atoms as the conventional cell shown in **a** and **b** (Supplementary Section I). **c**, The bulk BZ and its projections onto the conventional-cell (001) and (110) surfaces. **d**, The electronic band structure of $(TaSe_4)_2I$ with spin-orbit coupling. Bands along ΓZ cross at the Fermi energy (E_F) near the halfway points $k_z=\pm\pi/c$—a remnant of a filling-enforced nodal plane that is present in the band structure of a crystal of decoupled $TaSe_4$ chains (Supplementary Section I). Away from the high-symmetry BZ lines, there are 48 WPs lying within the energy range $-10\,\text{meV} < (E-E_F) < 15\,\text{meV}$ (Fig. 2), which we designate the FSWPs. The momentum-space coordinates and chiral charges of all 48 FSWPs are provided in Supplementary Section A, and characteristic band dispersions for each FSWP are provided in Supplementary Section B. Further below E_F, there are also eight C_{4z}-enforced chiral fermions (WPs) along ΓZ. As shown in the left inset of **d**, moving along ΓZ in increasing k_z, four of the eight C_{4z}-enforced WPs exhibit the compensating chiral charges +2, −1, +1 and −2 (their partners under $\mathcal{T}$ along ΓZ with negative values of k_z also exhibit the same charges, because $\mathcal{T}$ does not invert the chiral charge of a WP[1,37]). In the right inset of **d**, we show that bands along PN are gapped at E_F. **e**, Bands between the W_1^+ and W_4^- FSWPs (Fig. 2) are separated by a large non-trivial energy window of 0.123 eV, or on the order of 1,400 K.

ARPES and X-ray diffraction (XRD) experiments on $(TaSe_4)_2I$ samples to determine the gap, symmetry and modulation vectors of the CDW phase (Supplementary Section H). Our theoretical and experimental analyses suggest that $(TaSe_4)_2I$ is the first known material to host a correlation-driven Weyl semimetal–insulator phase transition.

Crystal structure. $(TaSe_4)_2I$ (Inorganic Crystal Structure Database[42] no. 35190, further details available at https://topologicalquantumchemistry.org/#/detail/35190[43,44]) crystallizes in a quasi-1D, body-centred tetragonal chiral structure in SG 97 ($I422$)[34]. The conventional cell of $(TaSe_4)_2I$ contains two $TaSe_4$ chains aligned along the c axis and four iodine atoms separating the chains (Fig. 1a,b). Each chain is formed of four alternating layers of Ta atoms and rectangles with four Se atoms on each corner, for a total of four Ta atoms and 16 Se atoms per chain. Within the conventional cell, there are two chains, implying a total chemical formula of $(TaSe_4)_8I_4$ per conventional cell (Fig. 1a,b). When decoupled, each chain exhibits exotic 'non-crystallographic' screw symmetries, which we detail further in Supplementary Section I. Because the crystal structure of $(TaSe_4)_2I$ is only generated by (body-centred) lattice translations and the proper rotation symmetries, C_{4z} and C_{2x}, where C_{ni} is a rotation by $360°/n$ about the i axis, then it is structurally chiral[37]. Additionally, because $(TaSe_4)_2I$ is nonmagnetic, its spectrum respects time-reversal ($\mathcal{T}$) symmetry. Because the monopole chiral charges (Chern numbers) of chiral fermions are left invariant under proper rotations and $\mathcal{T}$ (see ref. [11]), WPs in $(TaSe_4)_2I$ with opposite chiral charges are free to lie at different energies. Although an energy offset between oppositely charged chiral fermions has been predicted in Kramers–Weyl[37] and unconventional-fermion semimetals[38,45], $(TaSe_4)_2I$ presents a rare example of this energy offset in a conventional Weyl semimetal.

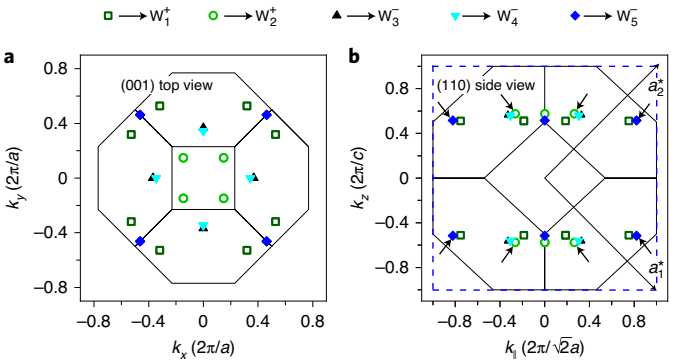

Fig. 2 | The distribution of FSWPs in the first bulk BZ. a,**b**, The distribution of FSWPs in the first bulk BZ, viewed from the top (001) (**a**) and side (110) (**b**) surfaces. In **b**, the FSWPs are concentrated in the vicinity of the $k_z=\pm\pi/c$ planes. The black lines in **a** and **b** represent the boundaries of 2D slices of the bulk BZ (Fig. 1c). In **b**, $a^*_{1,2}$ indicates the (110)-surface BZ primitive reciprocal lattice vectors (Supplementary Sections C and E), and the dashed blue box indicates the boundary of the second surface BZ (Supplementary Section C). In **a**, because of the bulk crystal symmetries, each symbol represents a pair of WPs with the same chiral charge lying at the opposite momenta $\pm k_z$ (Supplementary Section A). All of the symbols in **a** consequently represent FSWP projections with chiral charge $|C|=2$. In **b**, the relationship between the bulk WPs and symmetries is more complicated. We therefore use arrows to indicate which symbols in **b** correspond to the surface projections of only a single bulk FSWP (with charge $|C|=1$); in **b**, like in **a**, the symbols without arrows indicate the projections of two bulk FSWPs with the same chiral charge (for a net charge of $|C|=2$). The coordinates of the FSWPs are provided in Supplementary Section A.

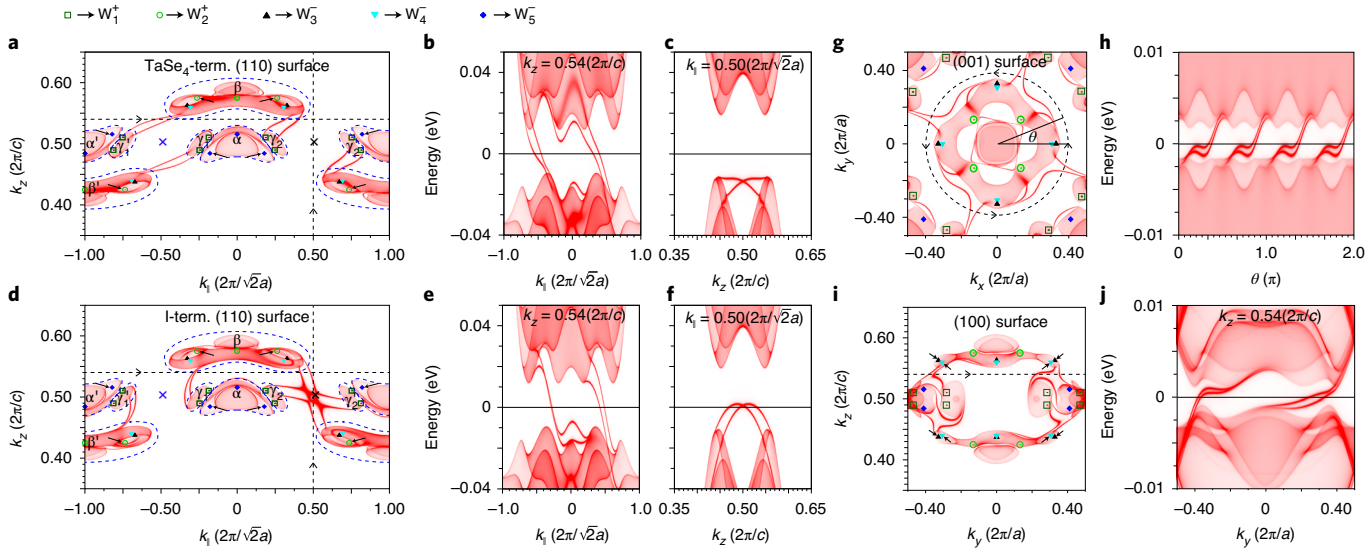

Fig. 3 | The surface states of $(TaSe_4)_2I$ terminated in the experimentally favoured[35] (110) direction, (001) direction and (100) direction. The labelling is as in Fig. 2. **a**,**d**, The (110) surface can be terminated with either $TaSe_4$ chains (Se-term.) or I atoms (I-term.). For both terminations of the (110) surface, the projections of the bulk states form four islands (and their time-reversal partners), which we enclose with blue dashed lines and label α (α′), β (β′), γ_1 (γ′) and γ_2 (γ′), respectively (Supplementary Sections A and C provide the definition of $k_{\|}$, the distribution of states within the full (110)-surface BZ and an examination of the surface projections of bulk states). The two × symbols in **a** and **d** represent surface TRIM points. The horizontal and vertical dashed lines in **a** and **d** indicate two cuts through the surface BZ at $k_z = 0.54(2\pi/c)$ and $k_{\|} = 0.50(2\pi/\sqrt{2}a)$, respectively. **b**,**c**,**e**,**f**, For both the Se- and I-terminations, the horizontal cut at $k_z = 0.54(2\pi/c)$ exhibits Chern number $C = -4$ (**b**,**e**), while the vertical cut at $k_{\|} = 0.50(2\pi/\sqrt{2}a)$ exhibits a trivial Chern number ($C = 0$) (**c**,**f**). The trivially connected surface states in **c** and **f** both intersect in two-fold linear crossings that are protected by $\mathcal{T}$-symmetry. In **d** and **f**, the I-termination surface atoms pull the trivial crossing in **c** towards the Fermi energy, and drive the four surface Fermi arcs at $k_{\|} > 0$ to merge in a surface Lifshitz critical point between a topological Fermi-arc connectivity linking the β and γ′ islands and a connectivity linking the β and γ_2 islands. Additionally, in **d**, the Fermi arcs that previously connected γ_1 and β′ (and their time-reversal partners) in **a** instead connect γ_1 to β (and γ′ to β′). **g**–**j**, Topological Fermi arcs are also present on the (001) surfaces (**g**,**h**) and (100) surfaces (**i**,**j**). In particular, like in the RhSi family[16–21,37,38,47], the (001)-surface Fermi arcs span the entire BZ (**g**), and the projected Fermi pockets at $k_{x,y} = 0, \pi/a$ exhibit large Chern numbers ($|C| = 8$) (**h**).

Electronic structure. Owing to its quasi-1D crystal structure, $(TaSe_4)_2I$ exhibits a strongly anisotropic electronic structure. In Fig. 1d, we show the band structure of $(TaSe_4)_2I$ calculated along high-symmetry lines in the first Brillouin zone (BZ) (Fig. 1c). We correspondingly observe weak dispersion in the $k_z = \pi/c$ plane along PN, and observe much stronger dispersion along ΓZ, as k_z is reciprocal to the chain translation direction c (z). We observe that there is a 1 eV gap in the $k_z = 0, 2\pi/c$ planes, whereas there is no band-gap in the vicinity of the $k_z = \pm\pi/c$ planes. In fact, we find that the entire Fermi surface of $(TaSe_4)_2I$ in SG 97 is localized near $k_z = \pm\pi/c$. This is surprising, because, in SG 97, generic points in the $k_z = \pm\pi/c$ planes are not fixed by symmetry, as they would be in a primitive tetragonal structure with a periodicity of c in the z direction (further WP symmetry analysis is provided in Supplementary Section A). In Supplementary Section I, we show that the localization of the Fermi surface can be understood by recognizing that $(TaSe_4)_2I$ is formed from weakly coupled screw-symmetric chains that individually exhibit symmetry- and filling-enforced nodal degeneracies near $k_z = \pi/c$.

Weyl point distribution. In 3D $(TaSe_4)_2I$, the entire Fermi surface is formed from topological bands connected to bulk chiral fermions (WPs). Specifically, because $(TaSe_4)_2I$ crystals in SG 97 ($I422$) are symmorphic, chiral and exhibit non-negligible spin–orbit coupling (SOC), all of their bulk degeneracies are necessarily point-like and carry non-trivial chiral charges, as explicitly shown in ref. [37] and discussed in Supplementary Section A. In the electronic structure of $(TaSe_4)_2I$ calculated from first principles, we observe 48 WPs within 15 meV of E_F (Fig. 2), which we designate as FSWPs, as well as eight C_{4z}-enforced chiral fermions (two pairs of conventional WPs and two pairs of double-WPs[26,46]) along ΓZ lying between 16 and 20 meV below E_F (left inset, Fig. 1d). In Supplementary Section I we detail the origin of the C_{4z}-enforced WPs in terms of the symmetry eigenvalues and band connectivity of isolated $TaSe_4$ chains. Because the C_{4z}-enforced WPs below E_F are only weakly separated ($\Delta k_z \approx 0.002(\frac{2\pi}{c})$) and carry a net-zero chiral charge within each narrow grouping, they are not likely to contribute experimentally detectable Fermi-arc surface states. Additionally, because all eight enforced chiral fermions are fully occupied and carry compensating chiral charges, they do not contribute to the bulk response or transport effects at intrinsic filling. Therefore, we will neglect the C_{4z}-enforced WPs below E_F in further discussions of the chiral fermions in $(TaSe_4)_2I$.

In Fig. 2a,b, we show (001)-surface (top) and (110)-surface (side) views, respectively, of the bulk FSWPs in the first BZ. The solid lines indicate the projected boundary of the first bulk BZ, and the differently shaped symbols each denote one set of symmetry-related FSWPs. Note that, although the FSWPs are distributed over a wide range in $k_{x,y}$ (Fig. 2a), they all lie within a close vicinity of the $k_z = \pm\pi/c$ planes (Fig. 2b). As shown in Supplementary Section I, this distribution of nodal points reflects that a crystal of decoupled $TaSe_4$ chains and iodine atoms is a filling-enforced semimetal with 4_2-screw- and $\mathcal{T}$-symmetry-enforced nodal surfaces that lie in the vicinity of the $k_z = \pm\pi/c$ planes.

Surface states. Weyl semimetals most notably exhibit characteristic topological Fermi-arc surface states. To confirm the presence of topological surface Fermi arcs in $(TaSe_4)_2I$, we calculated the surface states with surface Green's functions, as detailed in the Methods. $(TaSe_4)_2I$ is known to experimentally cleave on the conventional-cell

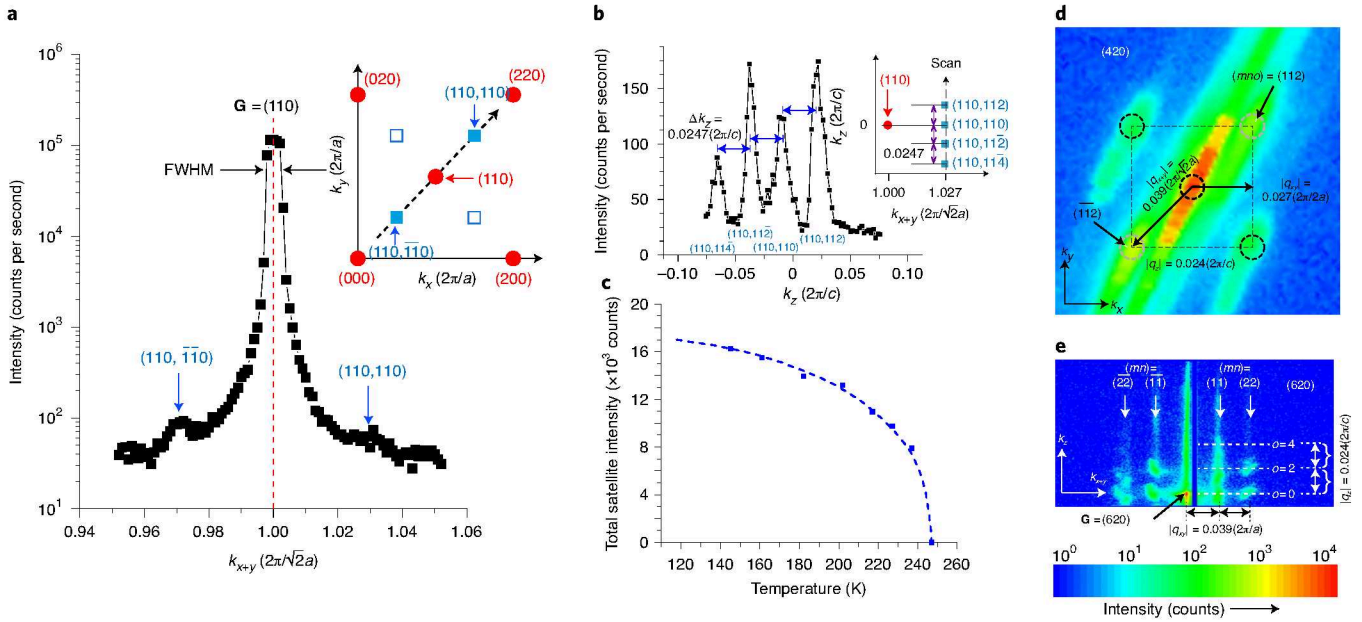

Fig. 4 | XRD data for the CDW phase of $(TaSe_4)_2I$. a, XRD line scan along the k_{x+y} direction through the **G** = (110) main reflection. FWHM indicates the full-width at half-maximum. **b**, XRD line scan along the k_z direction through the **Q** = (*hkl*, *mno*) = (110, 110) satellite reflection. **c**, Total measured satellite intensity in the vicinity of the **G** = (110) main reflection as a function of temperature. We observe that all satellites simultaneously disappear at $T_C \approx 248$ K, representing a signature of a transition away from a CDW phase. The measured T_C in **c** is slightly lower than, but still in close agreement with, the value of $T_C = 260$ K previously reported in refs. [39,40,49]. **d**,**e**, Two-dimensional reciprocal-space maps plotted on a logarithmic intensity scale and recorded near the **G** = (420) (**d**) and (620) (**e**) main reflections collected in the $k_{x,y}$ and $k_{x+y,z}$ planes, respectively. We attribute the elongated profile of the reflections in **d** and **e** to the logarithmic intensity scale and to the mosaicity of our sample, which we have measured through transverse angular scans to be 0.3° to 0.5°, well within the range of typical high-quality samples (~0.01° to ~1.0°, Supplementary Section H.1). In **b**, satellite reflections related by $C_{2,x+y}$ exhibit the same intensities. In **d**, pairs of satellite reflections related by C_{2z} (respectively labelled with white and dark dashed circles) exhibit the same intensities within uncertainty, but satellite reflections related by C_{4z} (for example, one satellite in a dashed white circle and one satellite in a dashed dark circle) exhibit intensities that differ by an order of magnitude. This implies that our sample contains two macroscopic domains with different, C_{4z}-related CDW orderings, where the CDW order within each domain respects the symmetries of point group D_2 (222) in a setting with C_{2z} and $C_{2,x\pm y}$ symmetry. The data for **a**, **b**, **d** and **e** were collected within a temperature range of roughly 88 K to 100 K, which is well below the sample critical temperature $T_C \approx 248$ K determined in **c**. Taken together, the XRD data imply that the CDW order within each of the domains in our sample would respect the symmetries of SG 22 (*F*222) or SG 16 (*P*222) if the underlying lattice were ignored or if the modulation vectors were tuned to a lattice-commensurate limit. Further details of our XRD experiments and CDW symmetry analysis are provided in Supplementary Section H.1.

(110) surface due to the weak van der Waals interactions between the $TaSe_4$ chains[34,35]. In Fig. 3, we show the calculated surface states of $(TaSe_4)_2I$ on the experimentally favourable (110) surface (Fig. 3a–f), as well as on the (001) and (100) surfaces (Fig. 3g,h and 3i,j, respectively).

The conventional-cell (110)-surface projections of the bulk Fermi surface of $(TaSe_4)_2I$ form four time-reversal pairs of separated islands in each surface BZ. In Fig. 3a,b, the islands (and their $\mathcal{T}$ partners) are enclosed with dashed blue lines and labelled as $\alpha\,(\alpha')$, $\beta\,(\beta')$, $\gamma_1\,(\gamma_1')$ and $\gamma_2\,(\gamma_2')$ (additional details are provided in Supplementary Section C). Each island is formed from the projected bulk Fermi pockets of the FSWPs, and can thus carry a total chiral charge. From the surface projections of the FSWPs, we infer that α, β, γ_1 and γ_2 carry the net chiral charges −4, −4, +4 and +4, respectively. Because the chiral charge of a WP does not change sign under $\mathcal{T}$ (see ref. [1]) then α', β', γ_1' and γ_2' also exhibit the same net charges of −4, −4, +4 and +4, respectively.

On both the $TaSe_4$-chain (Fig. 3a–c) and I-atom (Fig. 3d–f) terminations of the (110) surface of $(TaSe_4)_2I$, eight topological Fermi-arc surface states are present within each surface BZ. Like the bulk Fermi surface (Fig. 2b), the surface Fermi arcs are largely localized within a narrow k_z range near $k_z = \pm\pi/c$. To diagnose the topology of the surface Fermi arcs, we calculated the surface-state energy dispersion on closed loops traversing the (110)-surface BZ (horizontal and vertical cuts in Fig. 3a,d at $k_z = 0.54(2\pi/c)$ and $k_{\|} = 0.50(2\pi/\sqrt{2}a)$, respectively). On both the $TaSe_4$-chain and I-atom terminations, the horizontal cut (Fig. 3b,e, respectively) exhibits a $C = -4$ topological spectrum, and the vertical cut (Fig. 3c,f, respectively) displays a trivial spectrum. This can be understood by recognizing that the horizontal cut in Fig. 3a,d along $k_z = 0.54(2\pi/c)$ is equivalent to a loop around β. Conversely, the vertical cut in Fig. 3a,d, which lies along the projection of a $\mathcal{T}$-invariant bulk plane, is required to exhibit a net-zero Chern number. Consequently, on both possible terminations, no topological surface states cross E_F along the vertical line at $k_{\|} = 0.50(2\pi/\sqrt{2}a)$ (Fig. 3c,f). Interestingly, on the I-atom termination (Fig. 3d), the four surface Fermi arcs at $k_{\|} < 0$ exhibit a different connectivity than in Fig. 3a, and the four surface Fermi arcs at $k_{\|} > 0$ all intersect at a single time-reversal-invariant momentum (TRIM) point. Because the bulk projections and Fermi level in Fig. 3a,d are the same, we attribute the difference in Fermi-arc connectivity between Fig. 3a,d to surface Lifshitz transitions driven by the additional layer of (110)-surface I atoms that is present in Fig. 3d. In Supplementary Sections E and F, we respectively analyse the quasiparticle interference patterns and temperature dependence of the (110)-surface Fermi arcs.

Finally, although $(TaSe_4)_2I$ does not favour cleavage in the (001)-direction[35], the calculated (001)-surface Fermi arcs (Fig. 3g,h) still provide useful topological information. On the (001) surface, the projections of the bulk Fermi pockets lie close to $k_{x,y} = 0$, π/a and are connected by eight, zone-spanning topological Fermi arcs

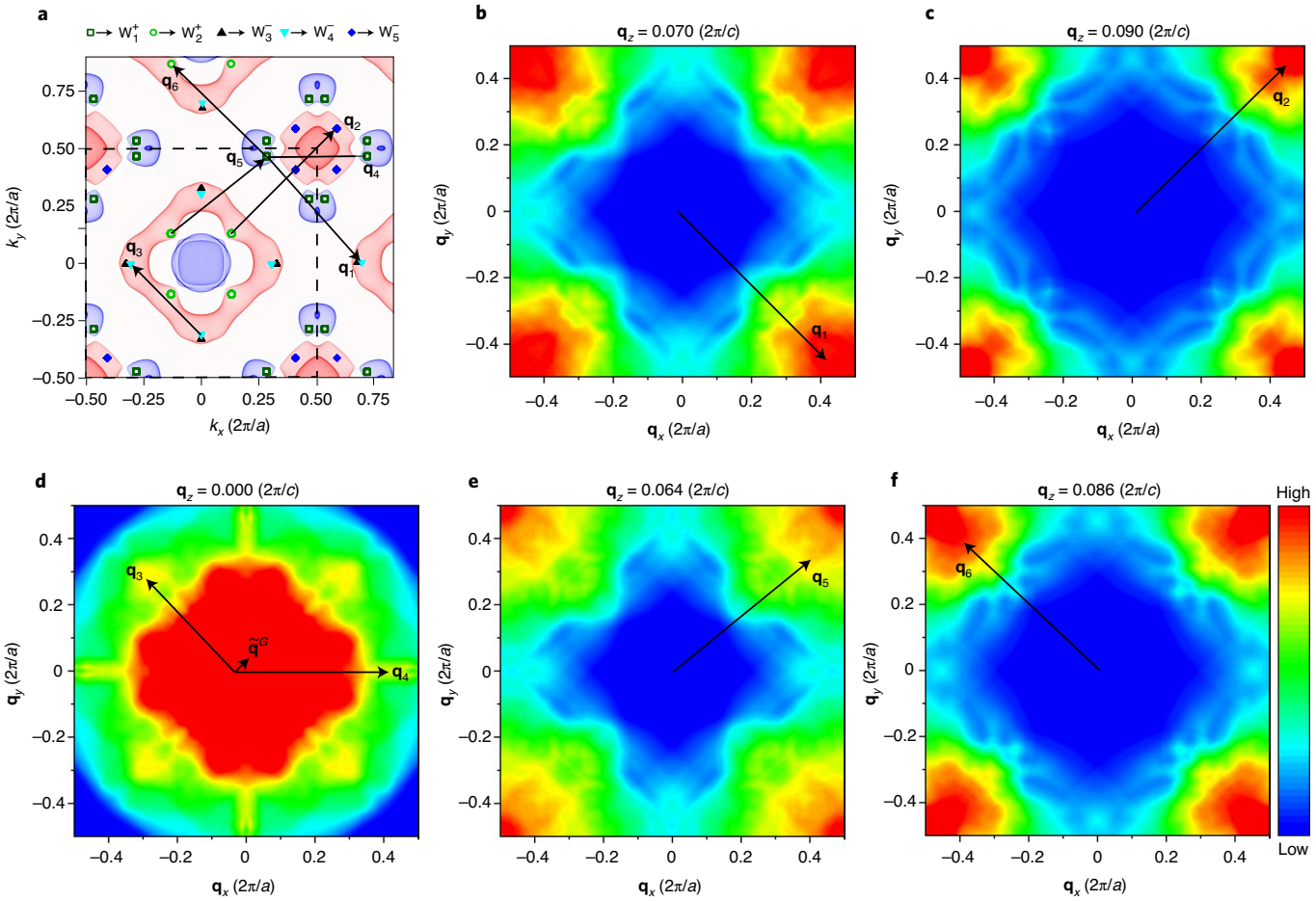

Fig. 5 | The (001) projection of the bulk Fermi surface of $(TaSe_4)_2I$ and the electronic susceptibility calculated from first principles. a, A top view ((001) projection) of the Fermi surface and the projected distribution of the FSWPs. Electron (hole) pockets are plotted in blue (red) and the FSWPs are labelled following the convention established in Fig. 2. The black dashed square in **a** indicates the boundary of the 3D conventional (second) BZ (Figs. 1 and 2). **b**–**f**, The electronic susceptibility $\chi_{\mathbf{q}}$ calculated using the Fermi surface in **a** at $\mathbf{q}_z = 0.070(\frac{2\pi}{c})$ (**b**), $\mathbf{q}_z = 0.090(\frac{2\pi}{c})$ (**c**), $\mathbf{q}_z = 0.000(\frac{2\pi}{c})$ (**d**), $\mathbf{q}_z = 0.064(\frac{2\pi}{c})$ (**e**) and $\mathbf{q}_z = 0.086(\frac{2\pi}{c})$ (**f**) (further calculation details are provided in Supplementary Section G). Up to symmetry-equivalent scattering vectors, the strong peaks shown in **b**–**f** represent all of the discernible peaks in $\chi_{\mathbf{q}}$ in the first 3D scattering BZ indexed by $q_{x,y,z}$ that coincide with FSWP nesting vectors (Table 1). We have also labelled the vector $\tilde{\mathbf{q}}^G$ within the large spot in **d** at $\mathbf{q}=\mathbf{0}$. $\tilde{\mathbf{q}}^G$ coincides with the $\mathbf{q}=(110)$ CDW modulation vector observed in our XRD experiments, which we emphasize to be much shorter than the FSWP nesting vectors in $(TaSe_4)_2I$ (Fig. 4 and Supplementary Sections G and H.1). This suggests that FSWP nesting is not itself the origin of the CDW in $(TaSe_4)_2I$. Nevertheless, we find that the high-density peaks $\mathbf{q}_i$ in $\chi_{\mathbf{q}}$—as well as the nesting vectors between all of the FSWPs in $(TaSe_4)_2I$ with opposite chiral charges (Supplementary Section A)—still match integer multiples of the experimentally observed CDW modulation vectors. This indicates that the CDW in $(TaSe_4)_2I$ backfolds and gaps the FSWPs, consistent with the appearance of a CDW gap in our ARPES experiments (Supplementary Section H.2).

(Fig. 3g). Calculating the (001)-surface states on a loop separating the projected Fermi pockets (Fig. 3h), we find that the projected Fermi pockets exhibit the largest Chern numbers thus far predicted ($|C|=8$). The (001)-surface states of chiral $(TaSe_4)_2I$ crystals are in this sense reminiscent of the experimentally confirmed large Fermi arcs of chiral crystals in the RhSi family[16–21,37,38,47], which also span the entire surface BZ and connect projected Fermi pockets with large Chern numbers.

Electronic susceptibility and experimental data. Having theoretically established that the high-temperature phase of $(TaSe_4)_2I$ is a Weyl semimetal, we will now demonstrate a relationship between the bulk FSWPs and the modulation vectors of the CDW phase. First, we performed experimental investigations of $(TaSe_4)_2I$ samples using XRD and ARPES probes to measure the CDW modulation vectors and gap, respectively (Supplementary Section H). Next, to characterize the electronic contribution to the CDW phase, we calculated the electronic susceptibility from first principles (Supplementary Section G). Finally, for comparison, we calculated the 'nesting' vectors between the FSWPs.

To begin, we first performed XRD experiments on single-crystal $(TaSe_4)_2I$ samples to infer the CDW modulation vectors and amplitude from satellite reflections. Specifically, when a crystal with the lattice constants a, b and c is periodically modulated, as occurs in a CDW phase, then satellite Bragg reflections begin to appear in XRD probes at the momentum-space locations $\mathbf{Q}=\mathbf{G}+\mathbf{q}$, where $\mathbf{G}=h\mathbf{a}^*+k\mathbf{b}^*+l\mathbf{c}^*$ are the larger reciprocal lattice vectors of the smaller unit cell of the unmodulated (high-temperature) structure, and $\mathbf{q}=m\boldsymbol{\eta}_1+n\boldsymbol{\eta}_2+o\boldsymbol{\delta}$ are the smaller modulation vectors of the (typically incommensurate) CDW-modulated structure. Examining the results of our XRD probes of $(TaSe_4)_2I$, we observed the appearance of satellite reflections in the vicinities of the $\mathbf{G}=(110)$, (420), (620) and (554) main reflections after samples were cooled below the sample critical temperature, $T_C \approx 248$ K (Fig. 4 and Supplementary

Table 1 | Data for the symmetry-equivalent sets of peaks in the electronic susceptibility that match FSWP nesting vectors

$\mathbf{q}_i$	Coordinates	Coupled	(m, n, o)	Re $(\chi_{\mathbf{q}_i})$
	$(q_x \frac{2\pi}{a}, q_y \frac{2\pi}{a}, q_z \frac{2\pi}{c})$	Weyl points		
$\mathbf{q}_1$	(0.41039, −0.46969, 0.07045)	$W_1^+ \rightarrow W_4^-$	(15, −17, 6)	151,945
$\mathbf{q}_2$	(0.45748, 0.45748, 0.09085)	$W_2^+ \rightarrow W_5^-$	(17, 17, 8)	235,822
$\mathbf{q}_3$	(−0.30640, 0.30643, 0.00000)	$W_4^- \rightarrow W_4^-$	(−11, 11, 0)	112,025
$\mathbf{q}_4$	(0.43364, 0.00000, 0.00000)	$W_1^+ \rightarrow W_1^+$	(16, 0, 0)	104,570
$\mathbf{q}_5$	(0.41496, 0.33791, 0.06479)	$W_2^+ \rightarrow W_1^+$	(16, 13, 5)	119,227
$\mathbf{q}_6$	(−0.41496, 0.39853, 0.08547)	$W_1^+ \rightarrow W_2^+$	(−15, 15, 7)	155,170
$\tilde{\mathbf{q}}^G$	(0.02700, 0.02700, 0.00000)	NA	(1, 1, 0)	691,542

Electronic susceptibility $\chi_{\mathbf{q}}$ is plotted in Fig. 5b–f and Supplementary Section G. Listed are the indices $\mathbf{q}_i$ of one vector within each symmetry-equivalent set of peaks in $\chi_{\mathbf{q}}$, the coordinates of $\mathbf{q}_i$ in the 3D conventional scattering BZ, the FSWPs nested by $\mathbf{q}_i$ (Supplementary Table 1), the closest integer multiple of the experimentally observed CDW modulation vectors $\mathbf{q} = (m, n, o) = m\boldsymbol{\eta}_1 + n\boldsymbol{\eta}_2 + o\boldsymbol{\delta} = [m\eta(\frac{2\pi}{a}), n\eta(\frac{2\pi}{a}), o\delta(\frac{2\pi}{c})]$, where $\eta = 0.027 \pm 0.001$ and $\delta = 0.012 \pm 0.001$ (further details are provided in Fig. 4 and Supplementary Section H.1), and the value of Re $(\chi_{\mathbf{q}_i})$ in relative units. Among the vectors listed in this table, $\mathbf{q}_1$ and $\mathbf{q}_2$ notably nest FSWPs with opposite chiral charges, and $\mathbf{q}_2$ is the strongest peak in $\chi_{\mathbf{q}}$ away from the large central spot near $\mathbf{q} = 0$ (Supplementary Section G). We have additionally listed the vector $\tilde{\mathbf{q}}^G$, which coincides with the high-intensity $\mathbf{q} = (110)$ satellite reflection observed in our XRD experiments (Supplementary Section H.1).

Section H.1), representing clear evidence of a CDW transition. The value of $T_C \approx 248$ K observed in our sample is slightly lower than, but still in close agreement with, the value of $T_C = 260$ K previously measured in $(TaSe_4)_2I$ (see refs. [39,40]). In the XRD data collected below T_C (Fig. 4a–e), we observe a tetragonal arrangement of satellite reflections whose modulation vectors (but not intensities) follow $\mathbf{q} = [m\eta(\frac{2\pi}{a}), n\eta(\frac{2\pi}{a}), o\delta(\frac{2\pi}{c})]$, where $m + n + o \in 2\mathbb{Z}$, $\eta = 0.027 \pm 0.001$ and $\delta = 0.012 \pm 0.001$ (further details are provided in Supplementary Section H.1).

However, through a careful analysis of the satellite reflection intensities in Supplementary Section H.1, we determined that our sample contains two macroscopic domains in position space in which the CDW exhibits a lower point group symmetry (D_2 (222) in a setting with C_{2z} and $C_{2,x\pm y}$ symmetries) than the high-temperature crystal structure in SG 97 ($I422$) (D_4 (422)). This can be seen from the XRD data shown in Fig. 4d, in which pairs of satellite reflections related by C_{2z} exhibit the same intensities within experimental uncertainty (Supplementary Section H.1), but satellite reflections related by C_{4z} exhibit intensities that differ by an order of magnitude. Isolating the satellite reflections within the domain of larger spatial volume—which we term the majority domain—we observe a pattern of satellite reflection vectors and intensities that would respect the symmetries of either SG 22 ($F222$) or SG 16 ($P222$) if the underlying lattice were ignored or if the modulation vectors were lengthened to a lattice-commensurate limit. Notably, the spacing of the satellite reflections in the $q_{x,y}$ plane (Fig. 4a,d,e) indicates that the CDW order is weakly 3D, consisting of both a Peierls-like modulation along the c axis, as well as weak modulation in the x–y plane. In Supplementary Section H.1, we use the intensities of the satellite reflections to obtain an estimate for the strength of the in-plane modulation, which we find to be small, but non-zero. We attribute the relative weakness of the in-plane CDW modulation to the weak van der Waals interactions between the $TaSe_4$ chains[34,35]. We emphasize that we were only able to obtain the CDW modulation vectors and estimate the magnitude of the in-plane CDW modulation because of the quality of our crystal sample and because of the high k- (q-) space resolution and dynamic intensity range of our experiments, which we further detail in Supplementary Section H.1.

Next, to characterize the electronic contribution of the Fermi surface of the high-temperature phase of $(TaSe_4)_2I$ to the low-temperature CDW phase[48–50], we calculated both the Fermi-surface nesting vectors between the FSWPs (Supplementary Section A), as well as the electronic susceptibility[51]. In Fig. 5b–f, we plot the real part of the bare electronic susceptibility in the constant-matrix approximation $\chi_{\mathbf{q}}$ (further details are provided in Supplementary Section G). To understand the origin of the peaks in $\chi_{\mathbf{q}}$, we compare the $\mathbf{q}$ vectors of the strong peaks to Fermi surface nesting vectors. We find that most—but not all—of the peaks in $\chi_{\mathbf{q}}$ match FSWP nesting vectors, and that the strongest peaks in $\chi_{\mathbf{q}}$ away from $\mathbf{q} = 0$ ($\mathbf{q}_2$ in Fig. 5c and Table 1) coincide with nesting vectors between FSWPs with opposite chiral charges. In Supplementary Section G, we detail the remaining peaks in $\chi_{\mathbf{q}}$, which are weaker than $\mathbf{q}_2$, but comparable in magnitude to $\mathbf{q}_{1,3-6}$ in Fig. 5b–f and Table 1. Furthermore, as shown in Fig. 4 and in Supplementary Section H.1, the CDW modulation vectors observed in our XRD experiments (for example, $\tilde{\mathbf{q}}^G$ in Fig. 5d) are much shorter than the FSWP nesting vectors, suggesting that FSWP nesting is not itself the origin of the CDW in $(TaSe_4)_2I$. Hence, our XRD and electronic susceptibility analyses provide further support for the recognition in ref. [51] that 3D CDWs rarely originate from electronic instabilities. Nevertheless, as shown in Supplementary Section A, because all of the nesting vectors between FSWPs with opposite chiral charges can be expressed as integer-valued linear combinations of the much shorter, majority-domain CDW modulation basis vectors (Supplementary Section H.1), then we conclude that the CDW in $(TaSe_4)_2I$ still backfolds and couples the FSWPs.

To further confirm that the CDW in $(TaSe_4)_2I$ opens an insulating gap, which has been measured in several previous studies[35,39,40], we performed ARPES probes of samples at 100 K and 270 K, which are respectively well below and above the CDW transition temperatures observed in our XRD experiments ($T_C \approx 248$ K, Fig. 4c) and in the aforementioned previous works ($T_C = 260$ K). In the low-temperature phase, we observe a gap of roughly 0.12 eV, which shrinks to less than 0.04 eV when samples are warmed to 270 K (additional details are provided in Supplementary Section H.2). We attribute this change in gap size to a transition from a low-temperature phase with a CDW-induced bandgap at all crystal momenta into the high-temperature Weyl-semimetal phase predicted in this work. Our ARPES experiments thus provide further evidence that the CDW couples all of the WPs with compensating chiral charges, because a gap cannot be opened by only coupling WPs with the same chiral charges[31–33].

Topology of the CDW gap. Because there are a large number of FSWPs, it is difficult to determine the precise topological nature of the CDW gap in $(TaSe_4)_2I$ at a static value of the CDW phase angle ϕ. However, it is plausible, and bolstered by recent experimental findings performed concurrently with this work[52], that the CDW gap is topologically non-trivial. Specifically, recent works have demonstrated that $\mathcal{T}$-symmetric Weyl-CDWs at fixed ϕ can be topologically equivalent to mean-field weak topological insulators whose weak-index vectors lie parallel to the CDW wavevector[53,54]. More generally, because we have shown that the CDW order in $(TaSe_4)_2I$ preserves two-fold rotation symmetries (Fig. 4 and Supplementary Section H.1), which, along with $\mathcal{T}$ symmetry, can protect a variety of topological crystalline insulating phases[55], then it is also possible that the CDW gap at static ϕ is topologically non-trivial in a manner distinct from previously studied Weyl-CDWs. This is further supported by analysing the high-temperature electronic structure of $(TaSe_4)_2I$ from the perspective of topological quantum chemistry[43] (Supplementary Section I). We leave for future study the

precise question of whether the CDW gap in $(TaSe_4)_2I$ accesses a lattice-incommensurate topological crystalline insulating phase with a single-particle description or whether the CDW accesses a more exotic, correlated topological phase beyond mean-field theory.

Online content

Any methods, additional references, Nature Research reporting summaries, source data, extended data, supplementary information, acknowledgements, peer review information; details of author contributions and competing interests; and statements of data and code availability are available at https://doi.org/10.1038/s41567-020-01104-z.

Received: 9 October 2019; Accepted: 23 October 2020;
Published online: 4 January 2021

References

1. Wan, X., Turner, A. M., Vishwanath, A. & Savrasov, S. Y. Topological semimetal and Fermi-arc surface states in the electronic structure of pyrochlore iridates. *Phys. Rev. B* **83**, 205101 (2011).
2. Weng, H., Fang, C., Fang, Z., Bernevig, B. A. & Dai, X. Weyl semimetal phase in noncentrosymmetric transition-metal monophosphides. *Phys. Rev. X* **5**, 011029 (2015).
3. Huang, S.-M. et al. A Weyl fermion semimetal with surface Fermi arcs in the transition metal monopnictide TaAs class. *Nat. Commun.* **6**, 7373 (2015).
4. Lv, B. Q. et al. Experimental discovery of Weyl semimetal TaAs. *Phys. Rev. X* **5**, 031013 (2015).
5. Xu, S.-Y. et al. Discovery of a Weyl fermion semimetal and topological Fermi arcs. *Science* **349**, 613–617 (2015).
6. Xu, S.-Y. et al. Discovery of a Weyl fermion state with Fermi arcs in niobium arsenide. *Nat. Phys.* **11**, 748–754 (2015).
7. Wang, Z. et al. $MoTe_2$: a type-II Weyl topological metal. *Phys. Rev. Lett.* **117**, 056805 (2016).
8. Sun, Y., Wu, S.-C., Ali, M. N., Felser, C. & Yan, B. Prediction of Weyl semimetal in orthorhombic $MoTe_2$. *Phys. Rev. B* **92**, 161107 (2015).
9. Soluyanov, A. A. et al. Type-II Weyl semimetals. *Nature* **527**, 495–498 (2015).
10. Jiang, J. et al. Signature of type-II Weyl semimetal phase in $MoTe_2$. *Nat. Commun.* **8**, 13973 (2017).
11. Vafek, O. & Vishwanath, A. Dirac fermions in solids: from high-T_c cuprates and graphene to topological insulators and Weyl semimetals. *Annu. Rev. Condens. Matter Phys.* **5**, 83–112 (2014).
12. Wang, Z. et al. Time-reversal-breaking Weyl fermions in magnetic Heusler alloys. *Phys. Rev. Lett.* **117**, 236401 (2016).
13. Armitage, N. P., Mele, E. J. & Vishwanath, A. Weyl and Dirac semimetals in three-dimensional solids. *Rev. Mod. Phys.* **90**, 015001 (2018).
14. Wang, Z., Weng, H., Wu, Q., Dai, X. & Fang, Z. Three-dimensional Dirac semimetal and quantum transport in Cd_3As_2. *Phys. Rev. B* **88**, 125427 (2013).
15. Wieder, B. J., Kim, Y., Rappe, A. M. & Kane, C. L. Double Dirac semimetals in three dimensions. *Phys. Rev. Lett.* **116**, 186402 (2016).
16. Bradlyn, B. et al. Beyond Dirac and Weyl fermions: unconventional quasiparticles in conventional crystals. *Science* **353**, aaf5037 (2016).
17. Schröter, N. B. M. et al. Chiral topological semimetal with multifold band crossings and long Fermi arcs. *Nat. Phys.* **15**, 759–765 (2019).
18. Takane, D. et al. Observation of chiral fermions with a large topological charge and associated Fermi-arc surface states in CoSi. *Phys. Rev. Lett.* **122**, 076402 (2019).
19. Sanchez, D. S. et al. Topological chiral crystals with helicoid-arc quantum states. *Nature* **567**, 500–505 (2019).
20. Rao, Z. et al. Observation of unconventional chiral fermions with long Fermi arcs in CoSi. *Nature* **567**, 496–499 (2019).
21. Schröter, N. B. M. et al. Observation and control of maximal Chern numbers in a chiral topological semimetal. *Science* **369**, 179–183 (2020).
22. Inoue, H. et al. Quasiparticle interference of the Fermi arcs and surface-bulk connectivity of a Weyl semimetal. *Science* **351**, 1184–1187 (2016).
23. Zheng, H. et al. Atomic-scale visualization of quantum interference on a Weyl semimetal surface by scanning tunneling microscopy. *ACS Nano* **10**, 1378–1385 (2016).
24. Sun, Y., Zhang, Y., Felser, C. & Yan, B. Strong intrinsic spin Hall effect in the TaAs family of Weyl semimetals. *Phys. Rev. Lett.* **117**, 146403 (2016).
25. Burkov, A. A. & Balents, L. Weyl semimetal in a topological insulator multilayer. *Phys. Rev. Lett.* **107**, 127205 (2011).
26. Xu, G., Weng, H., Wang, Z., Dai, X. & Fang, Z. Chern semimetal and the quantized anomalous Hall effect in $HgCr_2Se_4$. *Phys. Rev. Lett.* **107**, 186806 (2011).
27. de Juan, F., Grushin, A. G., Morimoto, T. & Moore, J. E. Quantized circular photogalvanic effect in Weyl semimetals. *Nat. Commun.* **8**, 15995 (2017).
28. Qi, X.-L., Hughes, T. L. & Zhang, S.-C. Topological invariants for the Fermi surface of a time-reversal-invariant superconductor. *Phys. Rev. B* **81**, 134508 (2010).
29. Li, Y. & Haldane, F. D. M. Topological nodal Cooper pairing in doped Weyl metals. *Phys. Rev. Lett.* **120**, 067003 (2018).
30. Li, Y. & Wu, C. The *J*-triplet Cooper pairing with magnetic dipolar interactions. *Sci. Rep.* **2**, 392 (2012).
31. Bobrow, E., Sun, C. & Li, Y. Monopole charge density wave states in Weyl semimetals. *Phys. Rev. Res.* **2**, 012078 (2020).
32. Wang, Z. & Zhang, S.-C. Chiral anomaly, charge density waves, and axion strings from Weyl semimetals. *Phys. Rev. B* **87**, 161107 (2013).
33. You, Y., Cho, G. Y. & Hughes, T. L. Response properties of axion insulators and Weyl semimetals driven by screw dislocations and dynamical axion strings. *Phys. Rev. B* **94**, 085102 (2016).
34. Gressier, P., Guemas, L. & Meerschaut, A. Preparation and structure of ditantalum iodide octaselenide, Ta_2ISe_8. *Acta Crystallogr. B* **38**, 2877–2879 (1982).
35. Tournier-Colletta, C. et al. Electronic instability in a zero-gap semiconductor: the charge-density wave in $(TaSe_4)_2I$. *Phys. Rev. Lett.* **110**, 236401 (2013).
36. Li, X.-P. et al. Type-III Weyl semimetals and its materialization. Preprint at https://arxiv.org/pdf/1909.12178.pdf (2019).
37. Chang, G. et al. Topological quantum properties of chiral crystals. *Nat. Mater.* **17**, 978–985 (2018).
38. Chang, G. et al. Unconventional chiral fermions and large topological Fermi arcs in RhSi. *Phys. Rev. Lett.* **119**, 206401 (2017).
39. Cava, R. J., Littlewood, P., Fleming, R. M., Dunn, R. G. & Rietman, E. A. Low-frequency dielectric response of the charge-density wave in $(TaSe_4)_2I$. *Phys. Rev. B* **33**, 2439–2443 (1986).
40. Maki, M., Kaiser, M., Zettl, A. & Grüner, G. Charge density wave transport in a novel inorganic chain compound, $(TaSe_4)_2I$. *Solid State Commun.* **46**, 497–500 (1983).
41. Zhang, Y., Lin, L.-F., Moreo, A., Dong, S. & Dagotto, E. First-principles study of the low-temperature charge density wave phase in the quasi-one-dimensional Weyl chiral compound $(TaSe_4)_2I$. *Phys. Rev. B* **101**, 174106 (2020).
42. *Inorganic Crystal Structure Database (ICSD)* (Fachinformationszentrum Karlsruhe, 2015).
43. Bradlyn, B. et al. Topological quantum chemistry. *Nature* **547**, 298–305 (2017).
44. Vergniory, M. G. et al. A complete catalogue of high-quality topological materials. *Nature* **566**, 480–485 (2019).
45. Liu, Q.-B., Qian, Y., Fu, H.-H. & Wang, Z. Symmetry-enforced Weyl phonons. *npj Comput. Mater.* **6**, 1–6 (2020).
46. Huang, S.-M. et al. New type of Weyl semimetal with quadratic double Weyl fermions. *Proc. Natl Acad. Sci. USA* **113**, 1180–1185 (2016).
47. Tang, P., Zhou, Q. & Zhang, S.-C. Multiple types of topological fermions in transition metal silicides. *Phys. Rev. Lett.* **119**, 206402 (2017).
48. Lorenzo, J. E. et al. A neutron scattering study of the quasi-one-dimensional conductor $(TaSe_4)_2I$. *J. Phys. Condens. Matter* **10**, 5039–5068 (1998).
49. Fujishita, H., Sato, M. & Hoshino, S. Incommensurate superlattice reflections in quasi one dimensional conductors, $(MSe_4)_2I$ (M = Ta and Nb). *Solid State Commun.* **49**, 313–316 (1984).
50. Lee, K.-B., Davidov, D. & Heeger, A. X-ray diffraction study of the CDW phase in $(TaSe_4)_2I$: determination of the CDW modulation amplitude. *Solid State Commun.* **54**, 673–677 (1985).
51. Johannes, M. D. & Mazin, I. I. Fermi surface nesting and the origin of charge density waves in metals. *Phys. Rev. B* **77**, 165135 (2008).
52. Gooth, J. et al. Axionic charge-density wave in the Weyl semimetal $(TaSe_4)_2I$. *Nature* **575**, 315–319 (2019).
53. Wieder, B. J., Lin, K.-S. & Bradlyn, B. Axionic band topology in inversion-symmetric Weyl-charge-density waves. *Phys. Rev. Res.* **2**, 042010(R) (2020).
54. Yu, J., Wieder, B. J. & Liu, C.-X. Dynamical piezomagnetic effect in time-reversal invariant Weyl semimetals with axionic charge-density waves. Preprint at https://arxiv.org/pdf/2008.10620.pdf (2020).
55. Fang, C. & Fu, L. New classes of topological crystalline insulators having surface rotation anomaly. *Sci. Adv.* **5**, eaat2374 (2019).

Methods

We performed ab initio calculations based on density functional theory as implemented in the FPLO package[56], and used the full-potential local-orbital basis within the generalized gradient approximation[57], fully incorporating the effects of SOC. The projected atomic Wannier functions (PAWFs) were constructed using the Ta *d*, Se *p* and I *p* orbitals to reproduce the band structures obtained from ab initio calculations. The surface states were obtained by calculating the surface Green's functions[58,59] of a semi-infinite tight-binding model constructed from the above PAWFs. All calculations were performed employing the experimental lattice parameters[34,60,61].

We also performed XRD and ARPES experiments on $(TaSe_4)_2I$ samples to study the CDW wavevector and electronic band structure, respectively. The XRD experiments were performed at beamline 25B of the European Synchrotron Radiation Facility in Grenoble, France using a six-circle diffractometer and a wavelength of $\lambda = 0.71$ Å. The whisker-shaped $(TaSe_4)_2I$ sample—which was ~100 µm in diameter and grown using the method detailed in ref. [52]—was first mounted on a copper sample holder oriented with its *c* axis perpendicular to the incoming beam and cooled to a minimum temperature of 88 K using a flow of liquid nitrogen. We then measured the intensities of the diffracted X-rays near several main Bragg reflections, employing a 2D pixel detector with pixel size of 55 µm placed 1,250 mm away from the sample to collect the data from both 1D line scans and 2D reciprocal-space maps. ARPES measurements were performed at the high-resolution branch of beamline I05 at the Diamond Light Source (DLS) with a Scienta R4000 analyser. The photon energy range for the DLS was 30–220 eV. The angles of the emitted photoelectrons were measured with a resolution of 0.2°, and their energies were measured at an overall resolution of <15 meV. After samples were glued to the sample holder, they were then cleaved in situ to expose the (110) surface, which is the favoured cleavage plane of $(TaSe_4)_2I$ (see ref. [35]). Throughout our ARPES experiments, samples were kept at a pressure of $<1.5\times10^{-10}$ torr, and measurements of the low- and high-temperature phases of $(TaSe_4)_2I$ were performed at 100 K and 270 K, respectively.

Data availability

The source data for all of the figures in this work are available at https://dataverse.harvard.edu/dataset.xhtml?persistentId=doi:10.7910/DVN/FSRRE4. All other data supporting the findings of this study are available from the corresponding authors upon reasonable request.

Code availability

The source code for the calculations performed in this work is available from the corresponding authors upon reasonable request.

References

56. Koepernik, K. & Eschrig, H. Full-potential nonorthogonal local-orbital minimum-basis band-structure scheme. *Phys. Rev. B* **59**, 1743–1757 (1999).
57. Perdew, J. P., Burke, K. & Ernzerhof, M. Generalized gradient approximation made simple. *Phys. Rev. Lett.* **77**, 3865–3868 (1996).
58. Sancho, M. P. L., Sancho, J. M. L. & Rubio, J. Quick iterative scheme for the calculation of transfer matrices: application to Mo (100). *J. Phys. F* **14**, 1205–1215 (1984).
59. Sancho, M. P. L., Sancho, J. M. L., Sancho, J. M. L. & Rubio, J. Highly convergent schemes for the calculation of bulk and surface green functions. *J. Phys. F* **15**, 851–858 (1985).
60. Gressier, P., Meerschaut, A., Guemas, L., Rouxel, J. & Monceau, P. Characterization of the new series of quasi one-dimensional compounds $(MX_4)_nY$ (M = Nb, Ta; X = S, Se; Y = Br, I). *J. Solid State Chem.* **51**, 141–151 (1984).
61. Gressier, P., Whangbo, M. H., Meerschaut, A. & Rouxel, J. Electronic structures of transition-metal tetrachalcogenides $(MSe_4)_nI$ (M = Nb, Ta). *Inorg. Chem.* **23**, 1221–1228 (1984).

Acknowledgements

We thank B. Bradlyn, K. Franke, Y. Hu and J. C. Y. Teo for helpful discussions. The first-principles calculations of the electronic structure, electronic susceptibility and quasiparticle interference patterns of $(TaSe_4)_2I$ were supported by DOE grant no. DE-SC0016239. B.J.W. and B.A.B. were additionally supported by NSF EAGER grant no. DMR 1643312, NSF-MRSEC grants nos. DMR-2011750 and DMR-142051, Simons Investigator grant no. 404513, ONR grants nos. N00014-14-1-0330 and N00014-20-1-2303, the BSF Israel US Foundation grant no. 2018226, the Packard Foundation, the Schmidt Fund for Innovative Research and a Guggenheim Fellowship from the John Simon Guggenheim Memorial Foundation. Z.W. was supported by the National Natural Science Foundation of China (grant no. 11974395), the Strategic Priority Research Program of the Chinese Academy of Sciences (CAS; grant no. XDB33000000), the Center for Materials Genome, and the CAS Pioneer Hundred Talents Program. H.L.M. acknowledges financial support from DFG through the priority program SPP1666 (Topological Insulators). Technical support by F. Weiss is gratefully acknowledged. H.L.M. thanks the staff of the ESRF for their hospitality during his stay in Grenoble, and additionally acknowledges helpful interactions with G. Castro, J. Rubio-Zuazo, K. Mohseni and R. Felici during experiments performed at the ESRF. W.S., Y.S., Y.Z. and C.F. were supported by ERC Advanced grant no. 291472 'Idea Heusler', ERC Advanced grant no. 742068–TOPMAT and Deutsche Forschungsgemeinschaft DFG under SFB 1143. W.S. additionally acknowledges support from the Shanghai high-repetition-rate XFEL and extreme light facility (SHINE). Y.Q. acknowledges support by the National Natural Science Foundation of China (grant nos. U1932217 and 11974246). Some of the calculations were carried out at the HPC Platform of ShanghaiTech University Library and Information Services and at the School of Physical Science and Technology.

Author contributions

This project was conceived by Z.W. and B.A.B. The Weyl semimetal phase of $(TaSe_4)_2I$ was discovered by W.S., Z.W., C.F. and B.A.B. The first-principles calculations of the high-temperature electronic structure and electronic susceptibility of $(TaSe_4)_2I$ were performed by W.S., Y.Z., Y.S. and Z.W. The quasiparticle interference patterns of the surface Fermi arcs were computed by B.J.W., W.S. and Z.W. The FPLO package and the Wannier function interface for first-principles calculations were written by K.K. The theoretical analysis was performed by B.J.W., Z.W. and B.A.B. The single-crystal bulk samples were synthesized by Y.Q. The XRD experiments were performed by H.L.M., J.J., P.W. and S.P. The ARPES experiments were performed by Y.L., L.S., L.Y. and Y.C. The manuscript was written by B.J.W., W.S., H.L.M., Z.W. and B.A.B., with help from all authors.

Competing interests

The authors declare no competing interests.

Additional information

Supplementary information is available for this paper at https://doi.org/10.1038/s41567-020-01104-z.

Correspondence and requests for materials should be addressed to B.A.B. or Z.W.

Peer review information *Nature Physics* thanks Emil Bergholtz, Congjun Wu and the other, anonymous, reviewer(s) for their contribution to the peer review of this work.

Reprints and permissions information is available at www.nature.com/reprints.